



# Broadband convolutional processing using band-alignment-tunable heterostructures

Lejing Pi<sup>1,3</sup>, Pengfei Wang<sup>1,2,3</sup>, Shi-Jun Liang<sup>1,2,3</sup>, Peng Luo<sup>1</sup>, Haoyun Wang<sup>1</sup>, Dongyan Li<sup>1</sup>, Zexin Li<sup>1</sup>, Ping Chen<sup>1</sup>, Xing Zhou<sup>1</sup>✉, Feng Miao<sup>2</sup>✉ and Tianyou Zhai<sup>1</sup>✉

**Broadband convolutional processing is critical to high-precision image recognition and is of use in remote sensing and environmental monitoring. Implementing in-sensor broadband convolutional processing using conventional complementary metal-oxide-semiconductor technology is, however, challenging because broadband sensing and convolutional processing require the use of the same physical processes. Here we show that a palladium diselenide/molybdenum ditelluride van der Waals heterostructure can provide simultaneous broadband image sensing and convolutional processing. The band alignment between type-II and type-III heterojunctions of the photovoltaic heterostructure is gate tunable, and the devices exhibit linear light-intensity dependence for both positive and negative photoconductivity, as well as linear gate dependence for the broadband photoresponse. Our in-sensor broadband convolutional processing improves recognition accuracy for multi-band images compared with conventional single-band-based convolutional neural networks.**

Broadband convolutional processing (BCP) can be used to extract the key spectral and spatial features in remote sensing images acquired across multi-spectral bands from ultraviolet (UV) to near-infrared (NIR)<sup>1–9</sup>. The development of in-sensor BCP, where analogue multiply–accumulate operations are used to achieve low power consumption and small latency<sup>10–13</sup>, could have important implications for intelligent edge devices. However, it is challenging to implement in-sensor BCP with conventional complementary metal–oxide–semiconductor technology because the necessary simultaneous broadband sensing and convolutional processing require the use of the same physical process<sup>14</sup>.

Van der Waals (vdW) heterostructures created by stacking together atomically thin materials with different band structures has been used to design a diverse range of electronic and optoelectronic devices, with functionalities that extend conventional complementary metal–oxide–semiconductor systems<sup>15–23</sup>. Broadband optoelectronic devices including photovoltaic detectors<sup>24,25</sup>, room-temperature infrared photodetectors<sup>26–28</sup> and photonic non-volatile memories<sup>29</sup>, have been particularly created by using heterostructures made with two semiconductors having different bandgaps. The band structure at the interface of vdW heterostructures can also be gate tunable, which allows novel electronic devices to be created<sup>30–32</sup>, including transverse tunnelling field-effect transistors<sup>23</sup>, mid-infrared sensitive avalanche photodetectors<sup>33</sup>, terahertz photon-type up-conversion imaging devices<sup>34</sup> and reconfigurable logic and neuromorphic devices<sup>35</sup>. In-sensor BCP could, thus, be achieved with vdW heterostructures by exploring broadband photoresponses and gate-tunable band alignments.

In this Article, we report in-sensor BCP using palladium diselenide (PdSe<sub>2</sub>)/molybdenum ditelluride (MoTe<sub>2</sub>) vdW heterostructures. The vdW heterostructures have a gate-tunable positive and negative photoresponse, as well as a broadband linear gate-dependence photoresponsivity, which allows different types of convolutional processing for remote sensing images to be achieved.

We show that recognition accuracy for remote sensing images using our broadband convolutional neural network is improved compared with a single-band-based network. We also demonstrate in-sensor image processing operations including sharpness and edge enhancement.

## In-sensor BCP

Figure 1a illustrates the physical process of implementing BCP with a gate-tunable photovoltaic heterostructure photosensor. The proposed in-sensor BCP allows for fast and low-power processing of remote sensing images. To this end, the heterostructure devices in the sensor should exhibit a broadband gate-tunable photovoltaic response, and their photoresponsivity should depend linearly on the gate voltage. The device can be used to sense strong broadband signals, and it combines convolution operations to obtain pre-processed images at different wavelengths. Simultaneous broadband sensing and data pre-processing can be implemented based on a single readout operation, where the operating mechanism for implementing BCP is illustrated in Fig. 1b. The input broadband image can be represented by the incident light ( $P_i$ ) at different wavelengths. The output photocurrent ( $I_{ph}$ ) can be expressed as  $\sum_j R_j P_j$ ,

where  $R_j$  is the photoresponse of the pixel and can also be regarded as the weight value of broadband convolution<sup>36</sup>. The in-sensor BCP can be implemented when the  $R_j$  value for each pixel is set to certain positive and negative values (Fig. 1b, inset), where positive and negative values indicate the different directions of current<sup>36</sup>. In addition, according to the gate-tunable photoresponse of the device, the kernel value of each pixel can be tuned by the gate voltage ( $V_g$ ). Thus, the convolutional kernels can be reconfigured to achieve different kernels used for input broadband images. The weights used for the conversion process are encoded into the gate-voltage matrix. The output photocurrents correspond to the weighted pixels in the input broadband images and represent the processed images.

<sup>1</sup>State Key Laboratory of Material Processing and Die & Mould Technology, School of Materials Science and Engineering, Huazhong University of Science and Technology, Wuhan, People's Republic of China. <sup>2</sup>Institute of Brain-Inspired Intelligence, National Laboratory of Solid State Microstructures, School of Physics, Collaborative Innovation Center of Advanced Microstructures, Nanjing University, Nanjing, People's Republic of China. <sup>3</sup>These authors contributed equally: Lejing Pi, Pengfei Wang, Shi-Jun Liang. ✉e-mail: [zhoux0903@hust.edu.cn](mailto:zhoux0903@hust.edu.cn); [miao@nju.edu.cn](mailto:miao@nju.edu.cn); [zhaity@hust.edu.cn](mailto:zhaity@hust.edu.cn)

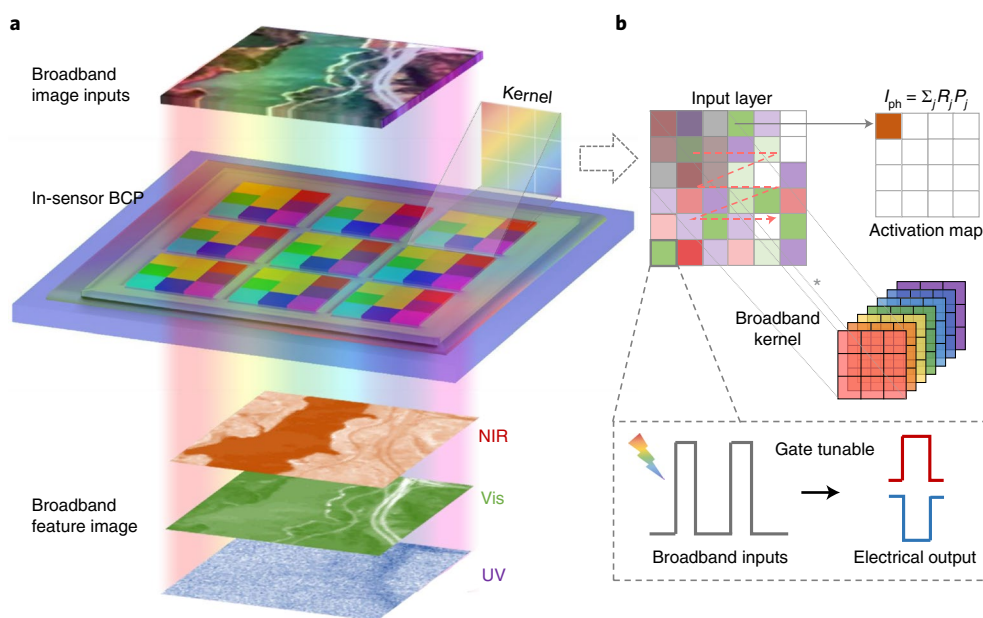


**Fig. 1 | Flow and mechanism for in-sensor BCP.** **a**, Schematic of image recognition using the in-sensor BCP (<https://rslab.ut.ac.ir/data>). **b**, Schematic of the mechanism for the broadband convolution calculation that derives a weighted electrical output from broadband optical inputs. The broadband kernel values can be represented by photoresponsivity ( $R_i$ ), which can be tunable by  $V_g$ . The input layer is represented by the incident light. The pixel values are equivalent to optical power ( $P_i$ ), and the output photocurrent can be represented with convolution operation  $\text{conv}(P_i, V_g)$ . The inset shows the concept of gate-tunable weights for each pixel that derives the weighted positive and negative photoresponsivity.

The individual pixel device in the image sensor is fabricated by using the mechanical exfoliation of high-quality single crystals and controllable dry transfer method to vertically stack two-dimensional (2D) PdSe<sub>2</sub> and MoTe<sub>2</sub> into a photovoltaic heterostructure (Fig. 2a), with the corresponding optical microscopy image shown in the inset of Fig. 2a. More details regarding device fabrication are provided in Methods. Due to their ambipolar nature and narrow bandgap, the photovoltaic heterostructure based on these two 2D materials exhibits a broadband response from UV to NIR<sup>3,37</sup>. Besides, the photoresponse can be modulated by applying an electrical field to engineer the band structure at the interface of the heterostructure, which is essential for realizing the in-sensor BCP<sup>3,37</sup>. The Raman and thickness characterizations of the PdSe<sub>2</sub> and MoTe<sub>2</sub> flakes are provided in Supplementary Fig. 1, and the high quality of the heterostructure is corroborated by the presence of an atomically sharp interface in the cross-sectional transmission electron microscopy images (Supplementary Fig. 2). We measured the electrical characteristics of the heterostructure device by varying the gate voltage. As shown in Supplementary Fig. 3, the  $I_{ds}-V_{ds}$  curve for the device exhibits the typical characteristic of a tunneling diode at a positive gate voltage, whereas a reverse rectifying behaviour can be observed at a negative gate voltage. The distinct rectifying properties of the PdSe<sub>2</sub>/MoTe<sub>2</sub> heterostructure device can be attributed to the difference in the built-in electric field under the distinct polarity of the gate voltage<sup>38</sup>. Under a negative gate bias, the Fermi level in PdSe<sub>2</sub> is shifted upward and a type-II band alignment is realized at the interface (Fig. 2e, left), leading to a built-in electrical field in the same direction as the applied forward bias. Under a positive gate voltage, the Fermi level shifts downward and a type-III or broken-gap band alignment is formed at the interface of the heterostructure (Fig. 2f, left), resulting in a blocked current flow through band-to-band tunnelling.

### Gate-tunable broadband photovoltaic effects

The gate-tunable band alignment in the PdSe<sub>2</sub>/MoTe<sub>2</sub> heterostructures gives rise to a broadband photovoltaic effect, which is

desirable for BCP. We characterized the broadband photovoltaic response under irradiation at different wavelengths (365 nm, 532 nm and 980 nm) by measuring the  $I_{ds}-V_{ds}$  curves at different gate voltages (namely, -10 V and 10 V), as shown in Fig. 2b. These results show the broadband photovoltaic effect from UV to NIR and the gate-tunable photovoltaic conversion between the second and fourth quadrants. According to the positive and negative directions of the short-circuit current ( $I_{sc}$ ), we define the photovoltaic phenomena in the second and fourth quadrants as positive and negative photovoltaic effects, respectively<sup>32</sup>. The positive and negative photocurrents generated in the device under 365 nm, 532 nm and 980 nm laser illumination are stable (Supplementary Fig. 4) and reproducible (Supplementary Fig. 5). Figure 2c,d displays the response speeds of the positive and negative photovoltaic effects under illumination at a wavelength of 980 nm. Both rising and falling times for the positive photoresponse are 0.4 μs, whereas the rising and falling times for the negative photoresponse are increased by one order of magnitude. Similarly, the device exhibits a fast photoresponse under illumination at 365 nm (Supplementary Fig. 6a,b) and 532 nm (Supplementary Fig. 6c,d). These results suggest that the device has no pronounced parasitic photomemory effect, which is another requirement for building fast broadband image sensors in addition to a broadband photoresponse.

We elucidate the working mechanism for the PdSe<sub>2</sub>/MoTe<sub>2</sub> heterostructure device under laser irradiation with different polarities of gate voltage. For all the measurements in this work, MoTe<sub>2</sub> (p type, terminal 's') was grounded. Under laser excitation, the carriers are generated in the heterojunction, as corroborated by the spatial-resolution photocurrent mapping (Supplementary Fig. 7). We also measured the bias and wavelength-dependent photocurrent profiles (Supplementary Fig. 8). Both results suggest that the gate-tunable photoresponse arises from the photovoltaic effect of the heterojunction, instead of asymmetric Schottky contacts. The distinct photoresponses under different polarities of gate voltage can be understood in the following. For the negative gate voltage (Fig. 2e), the built-in electric field in the heterojunction of type-II

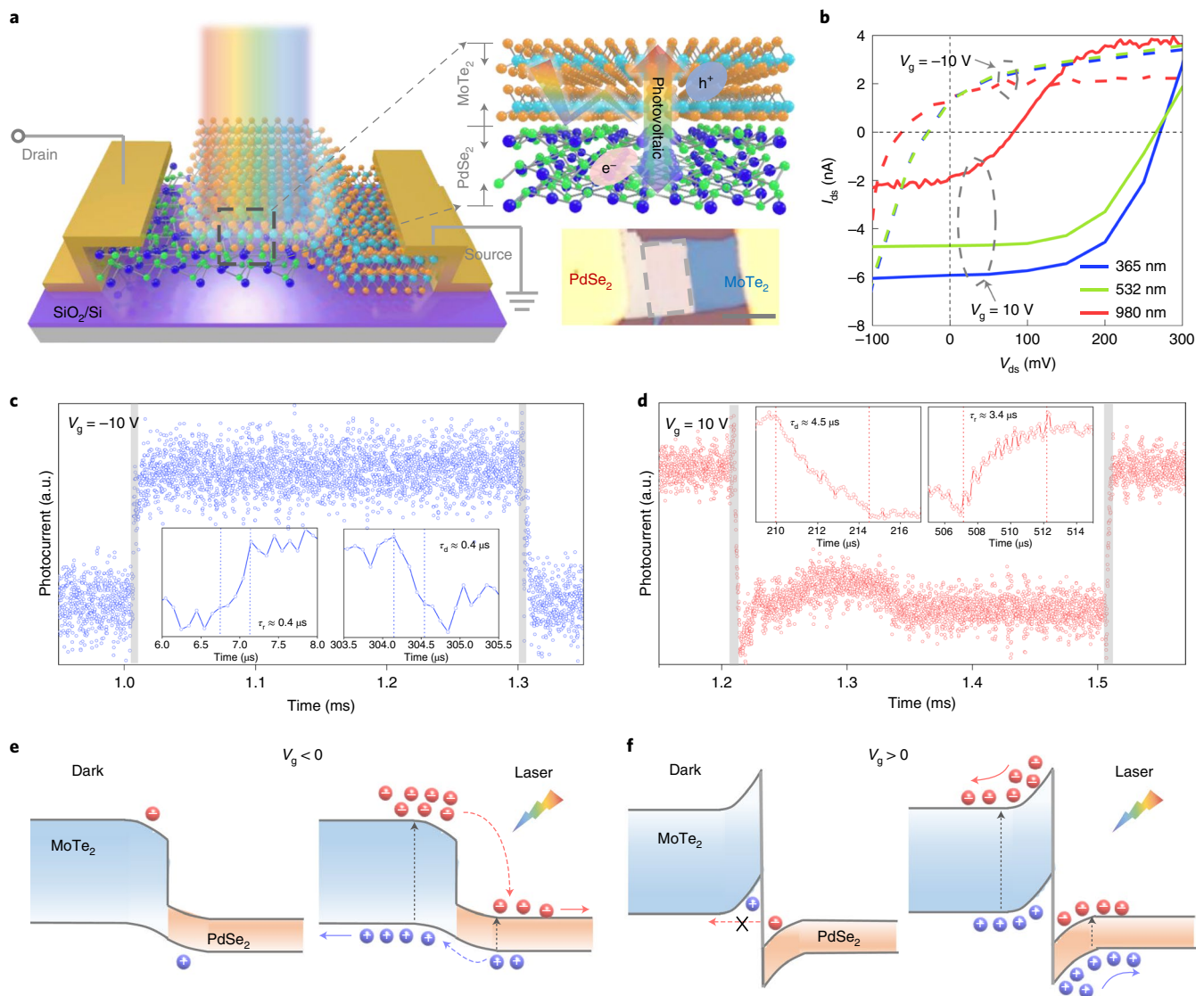


**Fig. 2 | Gate-tunable broadband positive and negative photovoltaic effects of PdSe<sub>2</sub>/MoTe<sub>2</sub> heterostructures.** **a**, Schematic of the PdSe<sub>2</sub>/MoTe<sub>2</sub> heterostructure device. The inset shows an optical image of the PdSe<sub>2</sub>/MoTe<sub>2</sub> heterostructure with area of  $\sim 9 \times 18 \mu\text{m}^2$ , and a schematic of the separation process for photogenerated carriers (hole, h<sup>+</sup>; electron, e<sup>-</sup>) at the interface of the heterostructure under laser illumination. Scale bars, 10  $\mu\text{m}$ . **b**, Positive and negative photovoltaic effects of the heterostructure device under different wavelengths (365 nm, 532 nm and 980 nm). **c, d**, Rise and fall times for positive (**c**) and negative (**d**) photovoltaic effects. To accurately determine the response speed of the device, a digital oscilloscope was utilized to record fast-varying photocurrent signals ( $\Delta T = 0.1 \mu\text{s}$ ). **e, f**, Band alignments for the PdSe<sub>2</sub>/MoTe<sub>2</sub> heterostructure and electron–hole pair generation in the negative (**e**) and positive (**f**) gate voltage.

band alignment points from n-type PdSe<sub>2</sub> to p-type MoTe<sub>2</sub>. With light illumination, both MoTe<sub>2</sub> and PdSe<sub>2</sub> absorb the incoming light and photocarriers are generated in close proximity to the junction. The photogenerated electron–hole pairs are instantly separated under the action of the built-in electric field to form the drift current. The resulting photocurrent flows towards the grounded terminal<sup>39</sup>, corresponding to the positive photocurrent observed in the second quadrant of Fig. 2b. In the case of a positive gate voltage (Fig. 2f), the resulting type-III band alignment blocks the drift of the carriers due to the existence of a tunnelling barrier. When illuminated with light, electron–hole pairs are generated in both MoTe<sub>2</sub> and PdSe<sub>2</sub> materials, and the photogenerated electrons in MoTe<sub>2</sub> and holes in PdSe<sub>2</sub> dominate the diffusion. The resulting diffusion current flows away from the grounded terminal<sup>38</sup>, corresponding to the measured photocurrent in the fourth quadrant of Fig. 2b.

### Linear photoresponse characteristics

Achieving BCP in photovoltaic heterostructure sensors requires a linear light intensity dependence and gate dependence for the broadband photocurrent. We measured the relationship between the broadband photoresponse and light intensity, as well as the gate voltage at different wavelengths. Figure 3a demonstrates the positive and negative photoresponses under different light intensities at a wavelength of 980 nm (indicated by shadow areas), and Fig. 3b presents the gate-tunable positive and negative photoresponses under fixed light intensities at a wavelength of 980 nm. To use the light intensity to represent the pixels in broadband images, it is desirable to have a linear intensity dependence on the photocurrent. We replot the power-dependent short-circuit photocurrent at different wavelengths and fit these curves with the formula  $I_{sc} \propto P^\alpha$  (Fig. 3c–e and Supplementary Fig. 9a,c). The fitted results show that the extracted values for  $\alpha$  are very close to 1 for all the wavelengths used

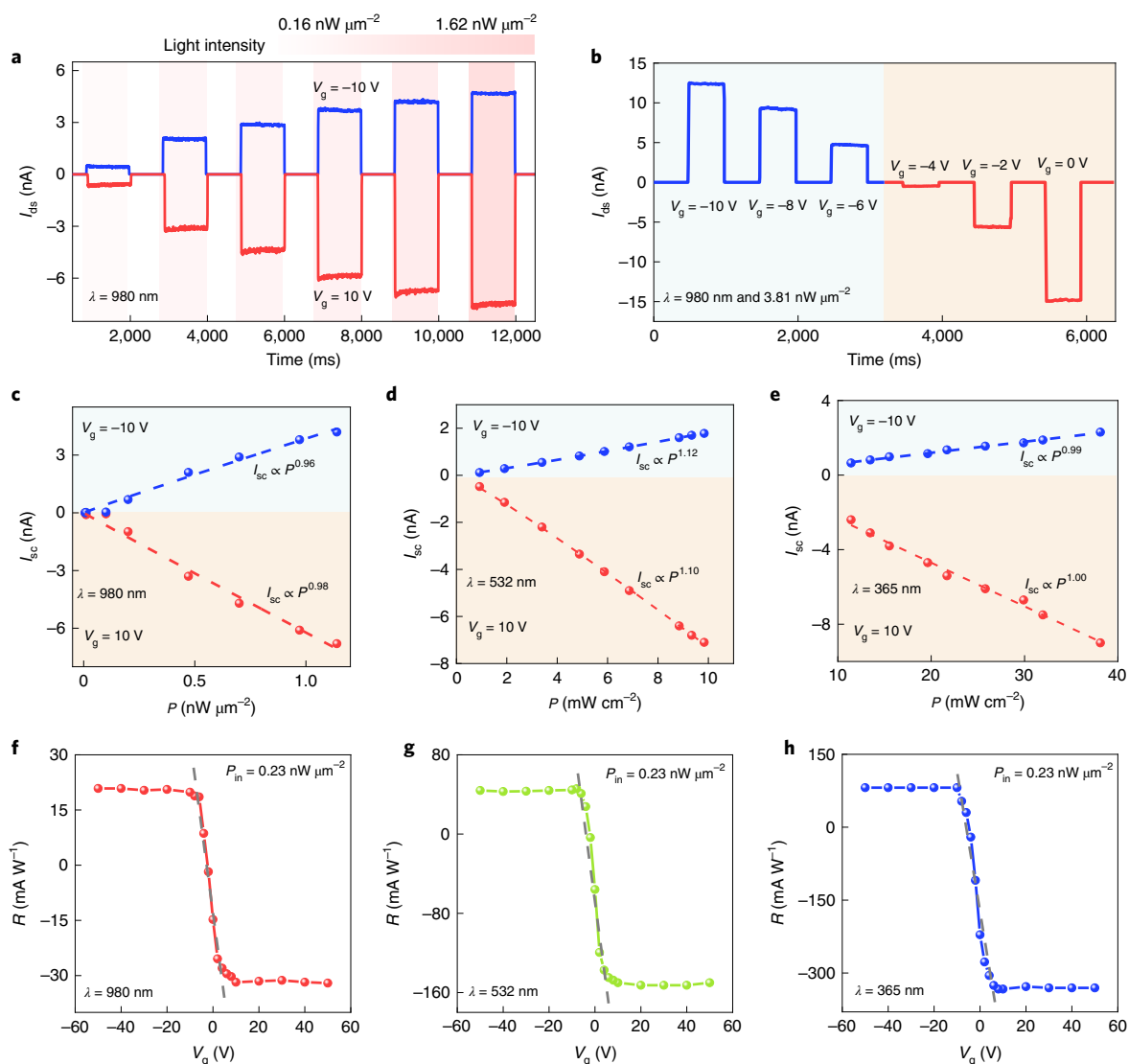


**Fig. 3 | Illustration of characteristics of PdSe<sub>2</sub>/MoTe<sub>2</sub> heterostructures for in-sensor BCP. **a**, Positive and negative photoresponses under different light intensities at a wavelength of 980 nm (indicated by shadow areas) at  $V_g = -10$  V and 10 V, respectively. **b**, Gate-tunable positive and negative photoresponse under illumination at 980 nm with a power density of  $3.81 \text{ nW } \mu\text{m}^{-2}$ . **c–e**, Light intensity dependence of the extracted short-circuit photocurrent for different gate voltages under light illumination of 980 nm (**c**), 532 nm (**d**) and 365 nm (**e**). The fitting shows a quasi-linear relationship, which is essential for representing the pixel greyscale with light intensity. **f–h**, Extracted photoresponse varies for 980 nm (**f**), 532 nm (**g**) and 365 nm (**h**), with gate voltages in the range from  $-50$  V to  $50$  V, and shows quasi-linear dependence. Under the same light intensity and gate voltage, the photoresponse for illumination at 980 nm, 532 nm and 365 nm is tunable from  $-35 \text{ mA W}^{-1}$  to  $20 \text{ mA W}^{-1}$ , from  $-160 \text{ mA W}^{-1}$  to  $50 \text{ mA W}^{-1}$  and from  $-350 \text{ mA W}^{-1}$  to  $100 \text{ mA W}^{-1}$ , respectively.**

in the experiment. The excellent linear mapping between the light intensity and photocurrent ensures the collection of high-quality image information. Similarly, we replot the experimental data for the gate-dependent positive and negative photoresponse for different wavelengths (Fig. 3f–h and Supplementary Fig. 9b,d), and fit these data to linear equations. The fitting results indicate that for the given wavelengths and light intensities, the photocurrent can be linearly varied by the applied gate voltage. Note that a linear window can be maintained for a voltage of  $\sim 10$  V. This characteristic not only allows for tuning the convolution kernels for various types of BCP but also enables the implementation of weight update in the training process of the convolutional neural network.

### Implementation of BCP

With the gate-tunable linear broadband photovoltaic effect of vdW heterostructure devices, we can implement various types of BCP with vdW photovoltaic heterostructure sensors. Under a fixed

gate voltage, the photoresponse modulation under different photon energies determines the wavelength-dependent convolution characteristics. In addition, the photoresponse depends on the gate voltage, and modulation of the gate voltage can be used to realize the configuration of different convolution kernels to achieve different operations on remote sensing images. As a proof of concept, we have used the single device to receive each pixel image one by one to perform the BCP. For demonstrating 2D broadband filtering or convolution operations, we have used hyperspectral images from Jasper Ridge datasets (Fig. 4a), which contains four end-members, namely, ‘road’, ‘soil’, ‘water’ and ‘tree’. It is worth noting that different types of information embedded in the hyperspectral image can be highlighted with different wavelength bands. The information for ‘soil’ and ‘tree’ is mainly highlighted within the NIR band, and ‘road’ and ‘water’ is mainly highlighted in the visible (Vis) band. However, in the UV band, the other features in the scene are completely absent, except for the high-contrast ‘road’. To



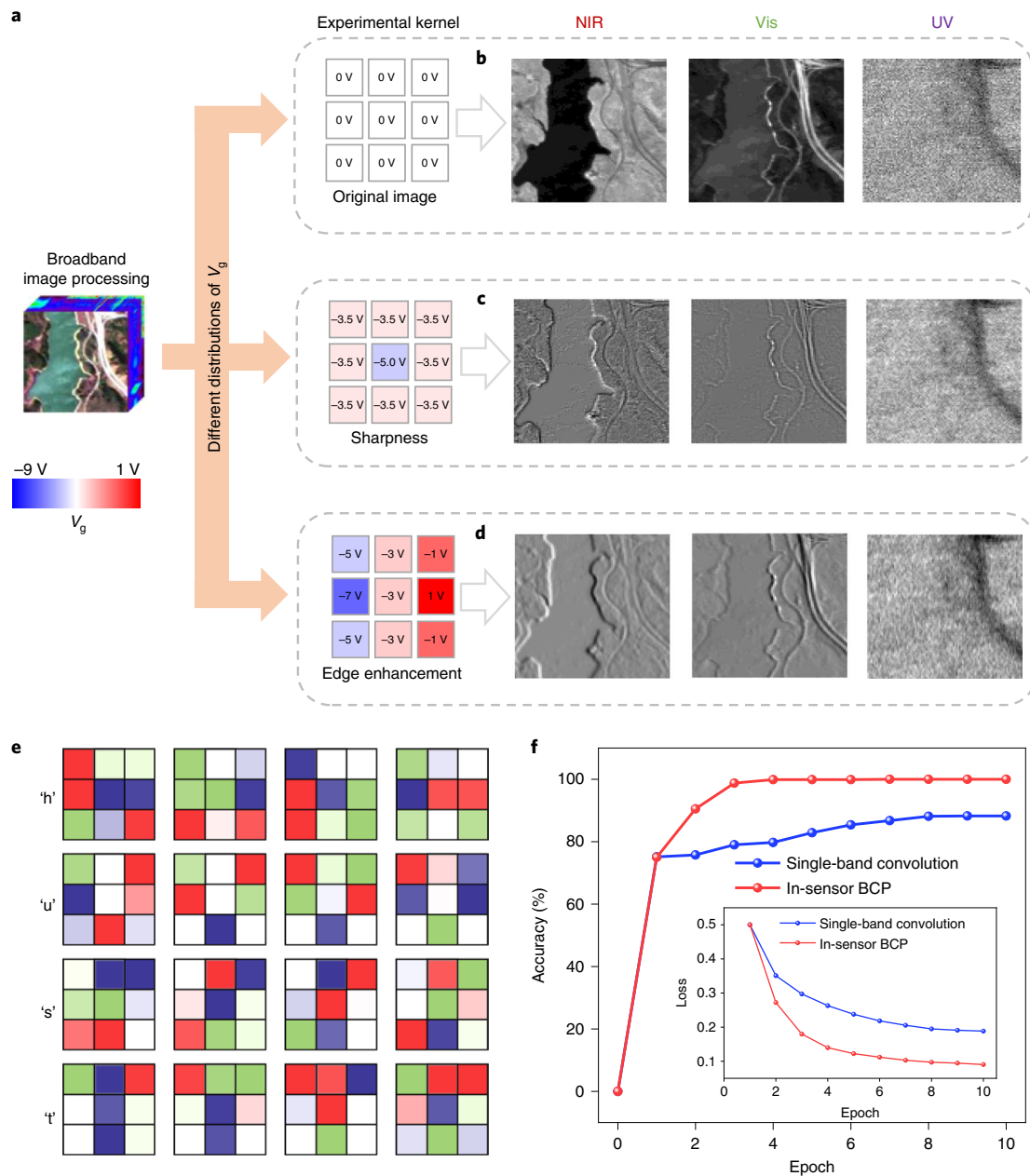


**Fig. 4 | Implementation of BCP with a vdW heterostructure photosensor.** **a**, Demonstration of different image processing operations (namely, edge enhancement and sharpness) with UV, Vis and NIR wavelengths. **b**, Original image. **c**, Sharpness. **d**, Edge enhancement. The realization of these functions by individually updating the gate voltage for heterostructure devices. The different colours in the array correspond to gate voltages. Hyperspectral image of the Jasper Ridge (<https://rslab.ut.ac.ir/data>). **e**, Typical broadband image of different types of letter ('h', 'u', 's' and 't'), where red, green and purple represent NIR (980 nm), Vis (532 nm) and UV (365 nm) light, respectively. To expand the amount of input data, Gaussian noise with a standard deviation of  $\sigma=0.2$  is uniformly added to the images as background noise, represented by different colours. **f**, Comparison of recognition accuracy between in-sensor BCP (red lines with dots) and single-band convolution network (blue lines with dots). The inset shows the loss function for in-sensor BCP and single-band convolution network.

filter the original hyperspectral images into individual wavelength bands, we divided the images into a series of  $3 \times 3$  sub-images (corresponding to a  $1 \times 9$  vector). Scanning the sub-images with our device without gating, we generate a series of discrete current values, which are representative of the input sequence. Figure 4b shows grey images produced by our device in the NIR, Vis and UV bands, similar to images achieved with conventional sensors that work in a single specific wavelength band. Furthermore, we can use our device to realize simultaneous sensing and BCP for the images such as sharpness and edge enhancement. Figure 4c,d

demonstrates the sharpness operation and edge enhancement for the images of different wavelength bands during image sensing with our devices. Compared with the original image shown in Fig. 4b, the sharpness of the image is realized by highlighting the hidden information for the underexposed/overexposed edges of the remote sensing scene (Fig. 4c). By modulating the gate voltage of the image sensor, we can implement the convolution kernels of edge enhancement to eliminate the contrast difference between the white background and black-scene patterns (Fig. 4d). The experimental data are in good agreement with the simulations,

which indicates that the vdW heterostructure photosensor is advantageous for remote sensing images (Supplementary Fig. 10). Furthermore, we demonstrate simultaneous sensing and processing of the Urban and Kennedy Space Center scenes with our vdW heterostructure photosensor (Supplementary Fig. 11).

Not limited to the application of BCP, the optoelectronic properties of the photovoltaic vdW heterostructure can be used to implement an in-sensor broadband convolution network and achieve higher recognition accuracy for broadband images over the single-band-based network. The training broadband image datasets are provided in Fig. 4e and Supplementary Fig. 12, including four different types of letter, namely, 'h', 'u', 's' and 't'. The training processes of BCP sensors for broadband pattern recognition and the corresponding training algorithm are provided in Supplementary Figs. 13a and 14. For the sake of simplicity, we have utilized the gate voltage to serve as weights in the kernels, since the gate-voltage dependence of photoresponsivity in individual devices is linear within a relatively wide region of gate voltage. The weight distribution of kernels is continuously optimized as the number of training epoch increases (Supplementary Fig. 15), which, in turn, increases the photocurrent (Supplementary Table 1). The target letters are recognized when the average output corresponding to the projected images is higher than the other output signals. In the experiment, we find that the strongest photocurrents from the broadband convolution neural network correspond well to the input broadband images (Supplementary Fig. 16). By measuring the average output at each epoch, the different target images can be classified (Supplementary Fig. 17). Compared with the single-band-based convolution neural network (Supplementary Fig. 13b), we demonstrate that the broadband convolution neural network can improve the recognition accuracy for broadband images under the same training conditions. Figure 4f shows the comparison of recognition accuracy between in-sensor broadband convolution network and single-band convolution network. The results show that the in-sensor broadband convolution network can reach nearly 100% recognition accuracy after three training epochs. A recognition accuracy of 90% is obtained with a single-band convolution network after ten training epochs. The advantage of the in-sensor broadband convolution network can also be manifested in the loss function (Fig. 4f, inset). Note the high recognition accuracy of the broadband images is mainly due to the fact that positive and negative photoresponsivities remain unchanged under different light intensities of distinct bands, which is an optoelectronic property of this heterostructure. This also means that thickness variations in 2D materials used in the BCP sensor have a negligible impact on the recognition accuracy. These results indicate that broadband convolution neural networks based on vdW heterostructure photosensors with gate-tunable band alignment have advantages over systems using photodiodes or phototransistors based on current thresholds.

Beyond the proof-of-concept demonstration in this work, the optimization of device structure and integration of device array are required to push the proposed concept towards practical applications. Memory could be introduced into the vdW heterostructures to create intelligent devices capable of performing in-memory sensing and in-memory computing, in addition to in-sensor computing. It is also important to develop more multi-wavelength processing strategies to extend the applications to hyperspectral sensing and processing<sup>40,41</sup>. Furthermore, combined with the progress in large-scale 2D materials<sup>42</sup> (for example, large-area films of MoTe<sub>2</sub> grown via seeded 2D epitaxy<sup>43</sup> and large-scale PdSe<sub>2</sub> films synthesized through the selenization of pre-deposited Pd films<sup>44</sup>) and the controllable transfer of 2D materials<sup>45</sup>, it should be possible in the future to achieve the large-scale integration of devices to implement practical convolution processing (Supplementary Fig. 18).

## Conclusions

We have reported in-sensor BCP using PdSe<sub>2</sub>/MoTe<sub>2</sub> vdW photovoltaic heterostructures, providing simultaneous broadband sensing and convolutional processing. The linear light intensity dependence and gate dependence of the broadband photocurrent allows us to use the vdW heterostructure sensor to implement a convolutional network for broadband image recognition and classification. Compared with a single-band-based convolutional network, the in-sensor BCP can effectively improve recognition accuracy. Our approach could be used to develop in-sensor BCP for various complex pattern recognition tasks.

## Methods

**Device fabrication.** Two-dimensional MoTe<sub>2</sub> (2D Semiconductors) and PdSe<sub>2</sub> (self-flux method<sup>46</sup>) flakes were obtained by a mechanical exfoliation approach. PdSe<sub>2</sub>/MoTe<sub>2</sub> heterostructures were fabricated by a controllable dry transfer method. First, few-layer PdSe<sub>2</sub> flakes were isolated from the corresponding bulk crystals onto a polydimethylsiloxane stamp and transferred to a 300 nm SiO<sub>2</sub>/Si substrate. Then, few-layer MoTe<sub>2</sub> flakes were exfoliated onto the polydimethylsiloxane stamp and transferred onto the PdSe<sub>2</sub> flakes through an aligned transfer system under an optical microscope. The source/drain electrodes (Cr/Au (10 nm/90 nm)) were patterned by adopting standard electron-beam lithography (FEI Quanta 650 and Raith ELPHY Plus) and thermal evaporation (Nexdep, Angstrom Engineering). To prevent the material from being affected by organic solvents, the electrodes were transferred to the heterostructures at a fixed point by an aligned transfer system. The vdW heterostructure devices have simple and compact structural characteristics.

**Device characterization.** The morphology and thickness of the PdSe<sub>2</sub>/MoTe<sub>2</sub> heterostructures were characterized by optical microscopy (BX51, Olympus) and atomic force microscopy (Dimension Icon, Bruker). Raman spectra were obtained by a confocal Raman system (alpha300 R, WITec) equipped with a 532 nm laser source. We conducted electronic measurements by using a probe station (TTPX, Lake Shore) equipped with a semiconductor device analyser (B1500A, Keysight). Meanwhile, the incident lights were provided with a laser-driven light source (EQ-1500, Energetiq). The fast time response was measured by using a semiconductor instrument (B1500A, Keysight) equipped with an ultrafast module (WGFMU) and a laser source operating at wavelengths of 365 nm, 532 nm and 980 nm.

**Implementation of pattern recognition.** To show that the BCP image sensor can be used for broadband image pattern recognition, the light signals representing the images were used as the input signal source, and the photocurrent value was given by  $I_{\text{output}} = \sum_{i=1}^9 \Delta I_{\text{sc}}^i$ . The measured photocurrent signals were then input to the sigmoid activation function to generate the outputs ( $f_1, f_2, f_3$  and  $f_4$ ), and the sigmoid activation function was defined as  $f = (1 + e^{-aI_{\text{output}}})^{-1}$ , where the scaling factor  $a = 1 \times 10^8 \text{ A}^{-1}$ . The error ( $\delta_p^k$ ) is obtained based on the feedback from the outputs,  $\delta_p^k = f_p^{(g)k} - f_p$ , where  $k$  represents the number of training images and  $p$  represents the number of input images. The error was further back-propagated to update the weight value  $\Delta V_g^k = \beta \times \text{round} \left( n^{-1} \sum_{p=1}^{p=40} a \times \text{conv} \left( P, \delta_p^k \right) \right)$ , where  $P$  is the input light intensity, step size  $\beta = 0.5 \text{ V}$  and the number of states  $n = 10$ .

## Data availability

The data that support the plots within this paper and other findings of this study are available from the corresponding authors upon reasonable request.

Received: 27 September 2021; Accepted: 17 March 2022;

Published online: 25 April 2022

## References

- Mennel, L. et al. Ultrafast machine vision with 2D material neural network image sensors. *Nature* **579**, 62–66 (2020).
- Zhou, F. et al. Optoelectronic resistive random access memory for neuromorphic vision sensors. *Nat. Nanotechnol.* **14**, 776–782 (2019).
- Seo, S. Y. et al. Reconfigurable photo-induced doping of two-dimensional van der Waals semiconductors using different photon energies. *Nat. Electron.* **4**, 38–44 (2021).
- Wu, C. et al. Programmable phase-change metasurfaces on waveguides for multimode photonic convolutional neural network. *Nat. Commun.* **12**, 96 (2021).
- Zhou, F. & Chai, Y. Near-sensor and in-sensor computing. *Nat. Electron.* **3**, 664–671 (2020).
- Feng, X., He, L., Cheng, Q., Long, X. & Yuan, Y. Hyperspectral and multispectral remote sensing image fusion based on endmember spatial information. *Remote Sens.* **12**, 1009 (2020).

7. Jameel, S. M., Hashmani, M. A., Rehman, M. & Budiman, A. Adaptive CNN ensemble for complex multispectral image analysis. *Complexity* **2020**, 8361989 (2020).
8. Jiang, J. H., Feng, X. A., Liu, F., Xu, Y. Y. & Huang, H. Multi-spectral RGB-NIR image classification using double-channel CNN. *IEEE Access* **7**, 20607–20613 (2019).
9. Ahmed, T. et al. Fully light-controlled memory and neuromorphic computation in layered black phosphorus. *Adv. Mater.* **33**, 2004207 (2021).
10. Roy, K., Jaiswal, A. & Panda, P. Towards spike-based machine intelligence with neuromorphic computing. *Nature* **575**, 607–617 (2019).
11. Zidan, M. A., Strachan, J. P. & Lu, W. D. The future of electronics based on memristive systems. *Nat. Electron.* **1**, 22–29 (2018).
12. Jayachandran, D. et al. A low-power biomimetic collision detector based on an in-memory molybdenum disulfide photodetector. *Nat. Electron.* **3**, 646–655 (2020).
13. Ham, D., Park, H., Hwang, S. & Kim, K. Neuromorphic electronics based on copying and pasting the brain. *Nat. Electron.* **4**, 635–644 (2021).
14. Choi, C. et al. Curved neuromorphic image sensor array using a MoS<sub>2</sub>-organic heterostructure inspired by the human visual recognition system. *Nat. Commun.* **11**, 5934 (2020).
15. Migliato Marega, G. et al. Logic-in-memory based on an atomically thin semiconductor. *Nature* **587**, 72–77 (2020).
16. Yu, J. et al. Bioinspired mechano-photonic artificial synapse based on graphene/MoS<sub>2</sub> heterostructure. *Sci. Adv.* **7**, eabd9117 (2021).
17. Pospischil, A., Furchi, M. M. & Mueller, T. Solar-energy conversion and light emission in an atomic monolayer p–n diode. *Nat. Nanotechnol.* **9**, 257–261 (2014).
18. Tao, Q. et al. Reconfigurable electronics by disassembling and reassembling van der Waals heterostructures. *Nat. Commun.* **12**, 1825 (2021).
19. Manzeli, S., Ovchinnikov, D., Pasquier, D., Yazyev, O. V. & Kis, A. 2D transition metal dichalcogenides. *Nat. Rev. Mater.* **2**, 17033 (2017).
20. Liu, Y. et al. Van der Waals heterostructures and devices. *Nat. Rev. Mater.* **1**, 16042 (2016).
21. Zhou, X. et al. Tunneling diode based on WSe<sub>2</sub>/SnS<sub>2</sub> heterostructure incorporating high detectivity and responsivity. *Adv. Mater.* **30**, 1703286 (2018).
22. Buscema, M. et al. Photocurrent generation with two-dimensional van der Waals semiconductors. *Chem. Soc. Rev.* **44**, 3691–3718 (2015).
23. Xiong, X. et al. A transverse tunnelling field-effect transistor made from a van der Waals heterostructure. *Nat. Electron.* **3**, 106–112 (2020).
24. Long, M. et al. Broadband photovoltaic detectors based on an atomically thin heterostructure. *Nano Lett.* **16**, 2254–2259 (2016).
25. Wu, D. et al. Highly polarization-sensitive, broadband, self-powered photodetector based on graphene/PdSe<sub>2</sub>/germanium heterojunction. *ACS Nano* **13**, 9907–9917 (2019).
26. Chen, Y. et al. Unipolar barrier photodetectors based on van der Waals heterostructures. *Nat. Electron.* **4**, 357–363 (2021).
27. Lukman, S. et al. High oscillator strength interlayer excitons in two-dimensional heterostructures for mid-infrared photodetection. *Nat. Nanotechnol.* **15**, 675–682 (2020).
28. Li, A. et al. Photodetectors: ultrahigh-sensitive broadband photodetectors based on dielectric shielded MoTe<sub>2</sub>/graphene/SnS<sub>2</sub> p–g–n junctions. *Adv. Mater.* **31**, 1970040 (2019).
29. Hu, L. et al. Phosphorene/ZnO nano-heterojunctions for broadband photonic nonvolatile memory applications. *Adv. Mater.* **30**, 1801232 (2018).
30. Jang, H. et al. An atomically thin optoelectronic machine vision processor. *Adv. Mater.* **32**, 2002431 (2020).
31. Baugher, B. W. H., Churchill, H. O. H., Yang, Y. & Jarillo-Herrero, P. Optoelectronic devices based on electrically tunable p–n diodes in a monolayer dichalcogenide. *Nat. Nanotechnol.* **9**, 262–267 (2014).
32. Lee, J. et al. Modulation of junction modes in SnSe<sub>2</sub>/MoTe<sub>2</sub> broken-gap van der Waals heterostructure for multifunctional devices. *Nano Lett.* **20**, 2370–2377 (2020).
33. Gao, A. et al. Observation of ballistic avalanche phenomena in nanoscale vertical InSe/BP heterostructures. *Nat. Nanotechnol.* **14**, 217–222 (2019).
34. Bai, P. et al. Broadband THz to NIR up-converter for photon-type THz imaging. *Nat. Commun.* **10**, 3513 (2019).
35. Pan, C. et al. Reconfigurable logic and neuromorphic circuits based on electrically tunable two-dimensional homojunctions. *Nat. Electron.* **3**, 383–390 (2020).
36. Wang, C.-Y. et al. Gate-tunable van der Waals heterostructure for reconfigurable neural network vision sensor. *Sci. Adv.* **6**, eaba6173 (2020).
37. Chow, W. L. et al. High mobility 2D palladium diselenide field-effect transistors with tunable ambipolar characteristics. *Adv. Mater.* **29**, 1602969 (2017).
38. Yan, R. et al. Esaki diodes in van der Waals heterojunctions with broken-gap energy band alignment. *Nano Lett.* **15**, 5791–5798 (2015).
39. Wu, F. et al. High efficiency and fast van der Waals hetero-photodiodes with a unilateral depletion region. *Nat. Commun.* **10**, 4663 (2019).
40. Merrill, R. B. Color separation in an active pixel cell imaging array using a triple-well structure. US patent 5,965,875 (1999).
41. Hubel, P. M., Liu, J. & Güttsch, R. J. Spatial frequency response of color image sensors: Bayer color filters and Foveon X3. In *Proc. SPIE Sensors and Camera Systems for Scientific, Industrial, and Digital Photography Applications V* Vol. 5301, 402–407 (SPIE, 2004).
42. Lin, Z. et al. 2D materials advances: from large scale synthesis and controlled heterostructures to improved characterization techniques, defects and applications. *2D Mater.* **3**, 042001 (2016).
43. Xu, X. et al. Seeded 2D epitaxy of large-area single-crystal films of the van der Waals semiconductor 2H MoTe<sub>2</sub>. *Science* **372**, 195–200 (2021).
44. Zeng, L. H. et al. Controlled synthesis of 2D palladium diselenide for sensitive photodetector applications. *Adv. Funct. Mater.* **29**, 1806878 (2019).
45. Quellmalz, A. et al. Large-area integration of two-dimensional materials and their heterostructures by wafer bonding. *Nat. Commun.* **12**, 917 (2021).
46. Pi, L. et al. Highly in-plane anisotropic 2D PdSe<sub>2</sub> for polarized photodetection with orientation selectivity. *Adv. Funct. Mater.* **31**, 2006774 (2020).

## Acknowledgements

This work was supported by the National Natural Science Foundation of China (grant nos. 52172144 (X.Z.), 21825103 (T.Z.), U21A2069 (T.Z.), 62122036 (S.-J.L.), 62034004 (F.M.) and 61974176 (S.-J.L.)), the Ministry of Science and Technology of China (2021YFA1200500 (X.Z.)) and the Strategic Priority Research Program of the Chinese Academy of Sciences (XDB44000000 (F.M.)). We also thank the Analytical and Testing Center at Huazhong University of Science and Technology for their support.

## Author contributions

L.P., X.Z., S.-J.L. and T.Z. conceived the concept and designed the experiments. L.P. prepared the heterostructures, performed the optoelectronic measurements and fabricated the devices with the help of X.Z. and P.C. D.L. and Z.L. performed the Raman and AFM characterizations. H.W., P.W. and P.L. designed the schematic. P.W., S.-J.L. and F.M. performed the BCP for the photosensor. All the authors analysed the data and wrote the manuscript together with discussion.

## Competing interests

The authors declare no competing interests.

## Additional information

**Supplementary information** The online version contains supplementary material available at <https://doi.org/10.1038/s41928-022-00747-5>.

**Correspondence and requests for materials** should be addressed to Xing Zhou, Feng Miao or Tianyou Zhai.

**Peer review information** *Nature Electronics* thanks the anonymous reviewers for their contribution to the peer review of this work.

**Reprints and permissions information** is available at [www.nature.com/reprints](http://www.nature.com/reprints).

**Publisher's note** Springer Nature remains neutral with regard to jurisdictional claims in published maps and institutional affiliations.

© The Author(s), under exclusive licence to Springer Nature Limited 2022